International Journal of Energy Research

WILEY

RESEARCH ARTICLE OPEN ACCESS

Enhancing Output Via Electron Transfer at Dielectric-Metal Interface in Triboelectric Nanogenerators

Minjung Chae[1,2] | June-Chul Shin[3,4] | Hee Jae Hwang[5]

[1]Biomaterials Research Center, Biomedical Research Division, Korea Institute of Science and Technology, Seoul 02792, Republic of Korea | [2]Department of Materials Science and Engineering, Seoul National University, Seoul 08826, Republic of Korea | [3]Department of Mechanical Engineering, Massachusetts Institute of Technology, Cambridge, Massachusetts, USA | [4]Research Laboratory of Electronics, Massachusetts Institute of Technology, Cambridge, Massachusetts, USA | [5]School of Mechanical Engineering, Kumoh National Institute of Technology (KIT), 61 Daehak-ro, Gumi 39177, Gyeongsangbuk-do, Republic of Korea

Correspondence: June-Chul Shin (semiron@mit.edu) | Hee Jae Hwang (hjhwang@kumoh.ac.kr)

Received: 20 November 2025 | **Revised:** 21 April 2026 | **Accepted:** 16 May 2026

Academic Editor: Puran Pandey

Keywords: dielectric-metal junction | electron transfer | TENGs | work function gap

ABSTRACT

Triboelectric nanogenerators (TENGs) operate fundamentally through electron transfer generated by contact electrification between positively and negatively charged materials and electrostatic induction to form electrical neutrality. This study investigated electron transfer at two critical interfaces: (i) between positively and negatively charged materials and (ii) between polydimethylsiloxane (PDMS), a negatively charged dielectric, and metal electrodes (Mg, Zn, and Ni) with distinct work functions. Band diagram analysis reveals that TENG with PDMS on Mg (TENG-PM) exhibited superior electrical output, attributed to the largest interfacial dielectric-metal junction gap (2.79 eV) at the dielectric-metal junction. To further enhance performance, Mg electrodes were micropatterned by abrasive polishing with #120, #600, and #1000 grit sandpapers, optimizing mechanical stress and facilitating electron transfer as confirmed by FEM simulations. The patterned Mg electrode with #120 grit sandpaper (TENG-PM [#120]) demonstrated the highest output, delivering voltages up to 679.89 V and currents of 20.35 μA, with a maximum power of 1.64 mW at a matching impedance of 10 MΩ, about 1.50 times higher than the unpatterned TENG-PM (1.09 mW at 6 MΩ). Capacitor charging tests and powering of 100 LEDs demonstrated the practical energy harvesting capability of the optimized devices. These results underscore the critical roles of work function alignment and controlled surface morphology in maximizing electron transfer and improving TENG performance, advancing the development of next-generation energy harvesters for diverse applications.

1 | Introduction

Building upon the growing demand for advanced energy harvesting systems, triboelectric nanogenerators (TENGs) have attracted significant attention as next-generation devices capable of efficiently converting external mechanical stimuli into electrical energy [1–3]. TENGs offer versatility in both design and material selection, making them well-suited for integration into wearable sensors, Internet of Things (IoT) platforms, and ocean monitoring applications, among others [4–6]. Recent advancements have focused on enhancing device output by adopting composite materials, employing substances [7, 8], and introducing micro/nanostructures at the material surface [9, 10], resulting in efficiency improvements by orders of magnitude over legacy systems.

The working mechanism of TENGs fundamentally centers on contact electrification occurring at the interface between the positively and negatively charged material [11, 12] and electrostatic induction to achieve electrical neutrality [13] during contact and separation cycles. Notably, recent studies have reported that negative triboelectric polymers and charge-excitation strategies can significantly enhance TENG output performance [14, 15].

Moreover, state-of-the-art research has demonstrated that output performance can be significantly improved by integrating ionic liquids [16], engineering charge-trapping interlayers [17], and patterning sophisticated micro- or nanostructures onto contact surfaces [18]. These strategies do not merely increase geometric contact area but also actively manipulate interfacial electronic dynamics, enabling precise control and enhancement of electron transfer between the active TENG layers as contact electrification, resulting in the enhancement of TENG output.

Among them, to moreover increase the output on TENGs, we could focus on the interface between the TENG layer and its electrode. In a previous study, Park et al. [19] demonstrated an electron blocking layer (EBL) to minimize electron screen out between an electrode and negatively charged material utilizing high permittivity materials. This study focused on the fundamental aspects of electron transfer across the TENG electrode-active material interface, systematically analyzing the underlying material and structural parameters and elucidating distinctive mechanisms for output enhancement.

In this study, we systematically examined the correlation between negatively charged materials and their electrodes with various work functions, emphasizing the underlying electron transfer mechanisms. Prior investigations established that electron transfer occurs from materials possessing a lower work function towards those with a higher work function, distinguishing electron donor and acceptor roles in triboelectric pairs [20]. Building on these insights, our work employed Kelvin probe force microscopy (KPFM) to probe the spatial distribution of surface potential at the PDMS-metal interface, which reflects the electronic equilibrium and charge redistribution resulting from work function-driven electron transfer. To further enhance interfacial electron transfer, micropatterning of electrodes was achieved by abrasion with sandpaper of distinct roughness levels, thereby engineering the surface morphology. Output performance for the TENG was systematically evaluated as a function of electrode roughness, alongside effective stress analysis of the negatively charged material. Our findings elucidate the optimum electrode configuration for maximizing electron transfer, contributing directly to substantial improvement in power generation efficacy within TENG devices.

2 | Results and Discussions

To evaluate electron transfer between the charged material and the electrode, three types of electrodes, with magnesium (Mg), zinc (Zn), and nickel (Ni), were selected. According to previous reports, the work functions of Mg, Zn, and Ni are 3.68, 4.3, and 5.01 eV, respectively [21, 22]. For the dielectric material, polydimethylsiloxane (PDMS) was chosen, exhibiting a work function of ~5.82 eV [17]. (Figure S2) Upon forming the metal–dielectric junction, band bending arises at the interface, driven by the work function difference between the metal and the polymer, in order to achieve electrical equilibrium.

To conduct a precise analysis of electron transfer between the charged materials and electrodes, we measured the work functions and Young's modulus (E) of Mg, Zn, and Ni, as shown in Figure 1a–c. The metal electrodes were fabricated by cutting 1 cm × 1 cm samples using a nanosecond-pulse laser. Work function values for Mg, Zn, and Ni were measured by KPFM as 3.03, 3.69, and 4.02 eV, respectively. Furthermore, the effective work functions of the PDMS-metal junctions are measured as 6.42 eV (PM), 6.09 eV (PZ), and 5.98 eV (PN), respectively, as shown in Figure 1e. Table 1 summarizes this hierarchy. The measured absolute values are systematically lower than UHV photoemission references (Mg: 3.68 eV, Zn: 4.3 eV, and Ni: 5.01 eV), reflecting the well-known sensitivity of ambient KPFM to native oxides and surface adsorbates [23, 24]. The relative ordering (Mg < Zn < Ni) and the work function differences between metals, which govern the band alignment in our analysis, are nevertheless preserved.

In a metal-dielectric junction, electrons redistribute from the lower work function metal to the higher work function dielectric (φ_{PDMS}: 5.82 eV), forming an interfacial dipole and band bending that creates a built-in potential ($\Delta V_{int} \approx \varphi_{PDMS} - \varphi_M$). This predicts the strongest electron transfer tendency for Mg ($\Delta\varphi = 2.79$ eV), followed by Zn (2.13 eV) and Ni (1.80 eV), which serves as the theoretical foundation for interpreting the subsequent surface potential and TENG output.

The surface charge is influenced by both capacitance and mechanical stress [7, 25, 26]. Enhancing these parameters in charged materials effectively increases the output performance of the TENG. To quantify this effect, we measured the stress–strain curves of the metal electrodes to extract their E. As shown in Figure 1a–c, iii), Ni exhibited the highest Young's modulus ($E = 421.32$ MPa), significantly exceeding those of Mg (203.36 MPa) and Zn (75.95 MPa). These mechanical properties, combined with later FEM analysis, help quantify the stress distribution at the PDMS-metal interface under identical loading conditions, providing insight into how local contact stress influences triboelectric charge density generation rather than directly probing electron transfer. Notably, the output hierarchy (TENG-PM > TENG-PZ > TENG-PN) is opposite to the modulus hierarchy (Ni > Mg > Zn), confirming that the electronic driving force dominates over the mechanical stiffness in this comparison.

Finally, we demonstrated the formation of metal–dielectric junctions via spin coating using PDMS, as illustrated in Figure 1d,e: PDMS-Mg (PM), PDMS-Zn (PZ), and PDMS-Ni (PN). These samples served as the negatively charged materials, while Ni fabric was employed as the positively charged material, as detailed in Figure S2. To solely compare electron transfer between PDMS and each metal electrode, Ni fabric and PDMS were fixed in place. The tests were conducted under a pressure of 25 kPa, a working frequency of 4 Hz, an active area of 4 cm^2, and a gap distance of 4 mm. Figure 1f–h show that the output performance of the TENG with PM (TENG-PM: 572 V, 15.9 μA, 38.2 nC) was superior to that of the TENG with PZ (TENG-PZ, 454 V, 14.8 μA, 32.5 nC) and the TENG with PN (TENG-PN, 399 V, 12.5 μA, 24.4 nC). These electrical outputs follow the same hierarchy as the KPFM surface potentials and theoretically predicted work function differences (Mg > Zn > Ni), establishing a clear correlation like Equation (1).

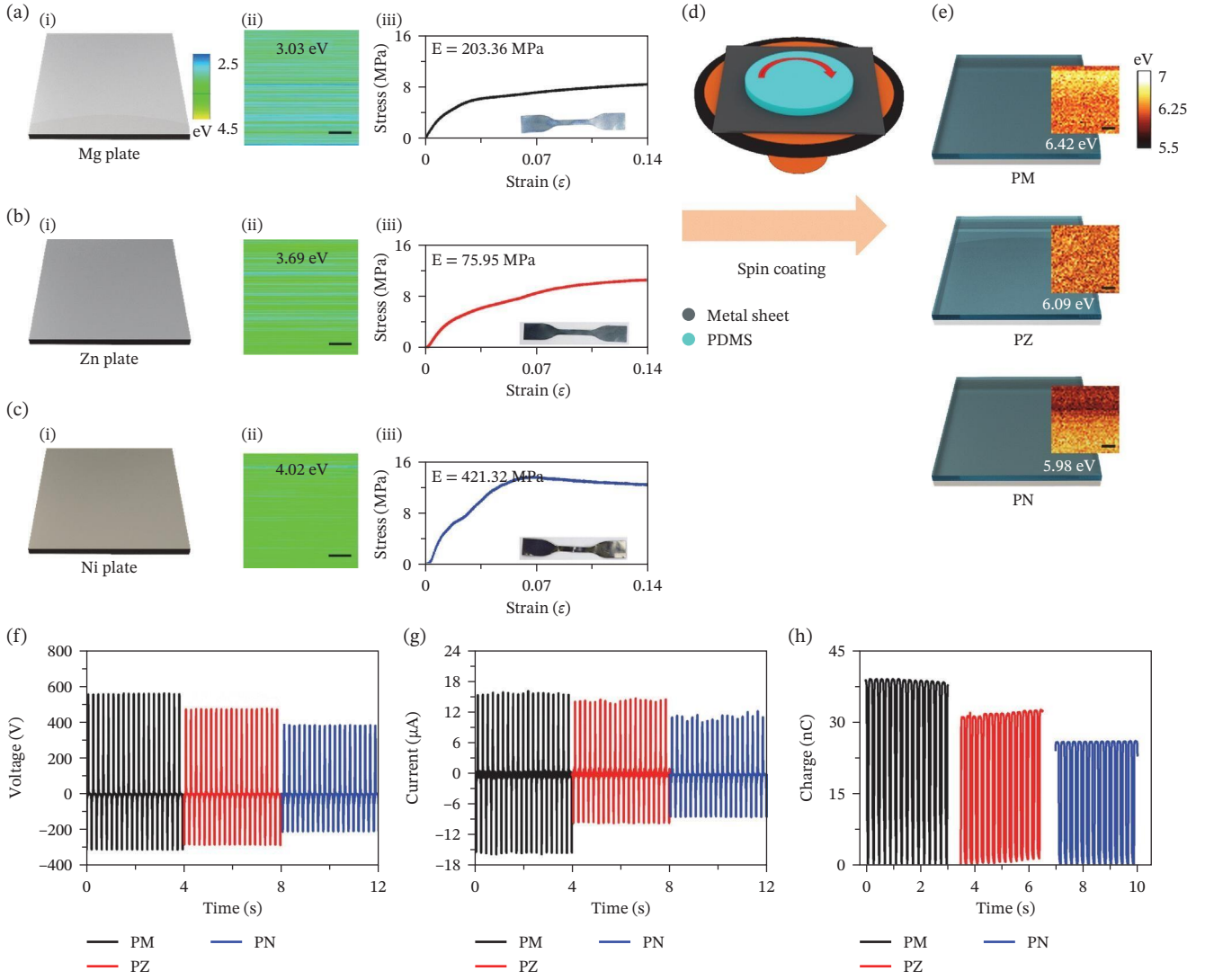

FIGURE 1 | Work function analysis of metal-PDMS junctions. (a–c) Mg, Zn, and Ni electrodes: i) plate geometry, ii) work functions (Mg: 3.03 eV, Zn: 3.69 eV, and Ni: 4.02 eV), and iii) Stress–strain curve with calculated Young's modulus (E). Scale bars in the KPFM maps represent 10 μm. (d) Process schematic for PDMS spin coating and (e) formation and work function of PM, PZ, and PN, establishing triboelectric series. Scale bars in the KPFM maps represent 10 μm. Output graphs: (f) voltage, (g) current, and (h) charge measured from TENG-PM, TENG-PZ, and TENG-PN.

TABLE 1 | Summary of metal work function (φ_{metal}), Young's modulus (E), effective PDMS work function on each metal ($\varphi_{PDMS,eff}$), friction-interface work function gap ($\Delta\varphi_1 = \varphi_{PDMS,eff} - \varphi_{Ni\ fabric}$) interfacial work function gap ($\Delta\varphi_2 = \varphi_{PDMS} - \varphi_{PDMS,eff}$, where $\varphi_{PDMS} = 5.82$ eV is the intrinsic PDMS work function), KPFM-measured surface potential (V_{SP}), and output voltage and current of TENG-PM, TENG-PZ, and TENG-PN.

Sample	φ_{metal}	E (MPa)	$\varphi_{PDMS,eff}$ (eV)	$\Delta\varphi_1$ (eV)	$\Delta\varphi_2$ (eV)	Surface potential (mV)	V (V)	I (μA)
PM	3.03 (Mg)	203.36 (Mg)	6.42	2.40	2.79	1261	572	15.9
PZ	3.69 (Zn)	75.95 (Zn)	6.09	2.07	2.13	686	454	14.8
PN	4.02 (Ni)	421.32 (Ni)	5.98	1.96	1.80	269	399	12.5

It is important to distinguish two work function gaps that jointly govern the TENG output. The friction layer gap $\Delta\varphi_1$ ($\Delta\varphi_1 = \varphi_{PDMS,eff} - \varphi_{Ni\ fabric}$) between the Ni fabric (4.02 eV) and the PDMS top surface (PM: 6.42, PZ: 6.09, PN: 5.98 eV) defines the triboelectric driving force at the contact interface, yielding $\Delta\varphi_1 = 2.40$, 2.07, and 1.96 eV for PM, PZ, and PN, respectively. The interfacial gap $\Delta\varphi_2$ ($\Delta\varphi_2 = \varphi_{PDMS} - \varphi_{metal}$) between the PDMS bulk (5.82 eV) and the backside metal (Mg: 3.03, Zn: 3.69, and Ni: 4.02 eV) drives band bending at the PDMS-metal junction and raises the PDMS effective work function above its intrinsic value. A larger $\Delta\varphi_2$ produces a larger upward shift of the PDMS surface work function, which in turn enlarges $\Delta\varphi_1$. Consequently, the triboelectric surface charge

density σ generated at the PDMS-Ni fabric contact is monotonically enhanced by $\Delta\varphi_1$, and the backside electrode governs σ through its modulation of $\varphi_{PDMS,eff}$ (Table 1). This coupling explains how the backside electrode, though not participating in the friction contact, controls the charge transfer dynamics at the top friction layer.

Figure 2 demonstrates electron transfer not only between positively and negatively charged materials but also between negatively charged materials and electrodes. Figure 2a–c display the KPFM surface potentials of pristine PM, PZ, and PN heterojunctions (without tribo-charging). The positive values reflect the backside-electrode-induced interfacial polarization: when a metal of lower work function is brought into contact with PDMS ($\varphi = 5.82$ eV), electron redistribution establishes an interfacial dipole that propagates a positive potential signature at the PDMS top surface. The magnitude of this signature scales with the metal-PDMS work function gap $\Delta\varphi^2$. In this configuration, KPFM effectively probes the electronic state of the entire PDMS/metal heterostructure at the top PDMS surface: although the PDMS composition is identical across PM, PZ, and PN, the effective work function at the PDMS top surface is modulated by the backside metal through the interfacial dipole, leading to the different measured CPD values. As the surface potential increases, the negative charge density on the material surface is enhanced [27]. The surface potential of PM (1261 mV) is significantly higher than those of PZ (686 mV) and PN (269 mV), demonstrating that the backside-electrode-induced interfacial polarization at the PDMS surface scales monotonically with $\Delta\varphi^2$ (Mg: 2.79 eV > Zn: 2.13 eV > Ni: 1.80 eV). All samples were charged under identical triboelectric contact conditions with Ni fabric (25 kPa, 4 Hz). This hierarchy (PM > PZ > PN) directly correlates with the work function differences measured in Figure 1a and predicted by the band alignment theory, validating KPFM surface potential as an effective indicator of interfacial charge transfer efficiency. This suggests that electron transfer from positively

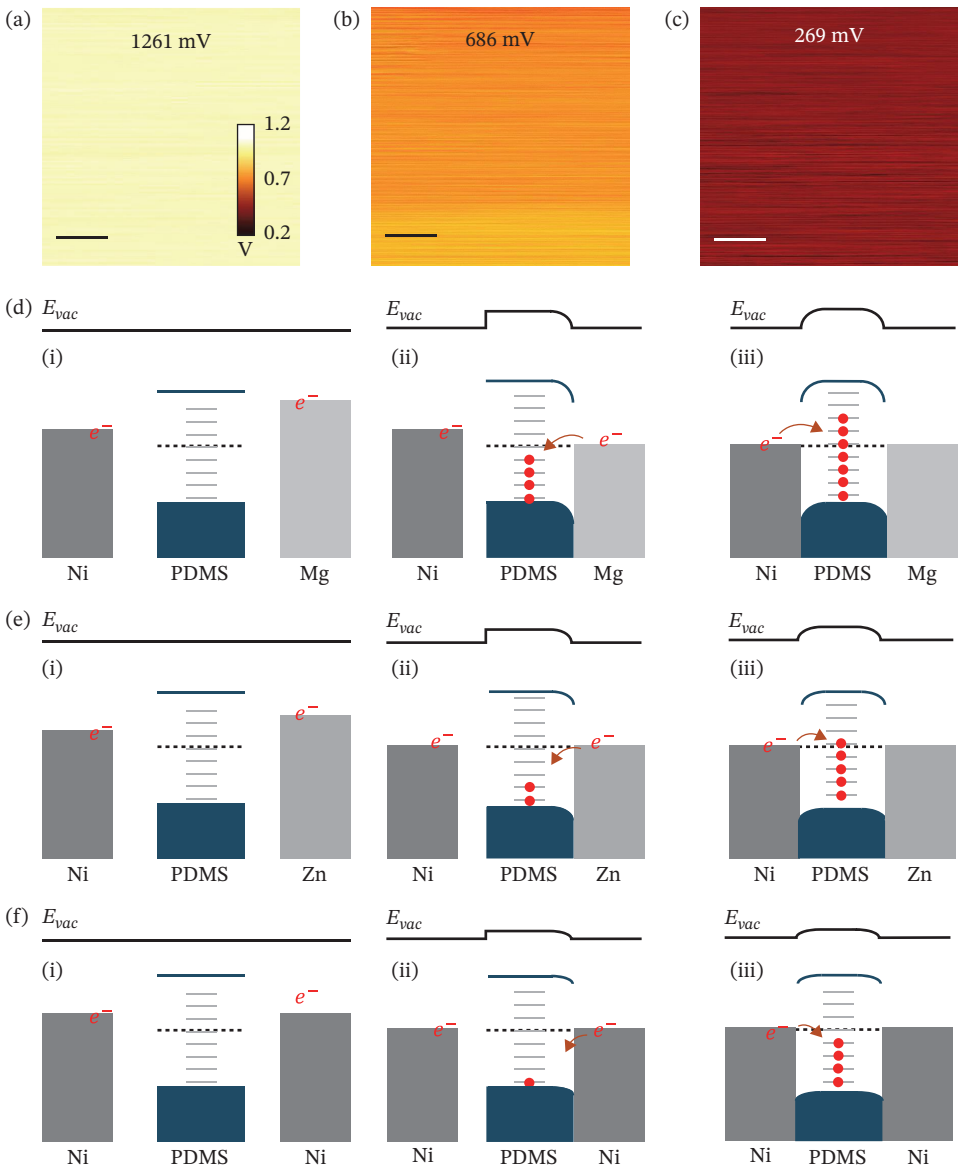

FIGURE 2 | Working mechanism of metal-dielectric structures in TENG. KPFM surface potential maps of pristine (a) PM, (b) PZ, and (c) PN heterojunctions, reflecting the backside-electrode-induced interfacial polarization at the PDMS surface. Scale bars represent 10 μm. Energy band diagrams of (d) TENG-PM, (e) TENG-PZ, and (f) TENG-PN are illustrated for three operational steps: i) before contact, ii) after contact, and iii) in contact (contact electrification).

charged materials and electrodes to PM is greater compared to the others, which is consistent with the observed output voltage, current, and charge measurements [28].

To further elucidate the detailed working mechanism of PM-TENG, PZ-TENG, and PN-TENG, energy level alignment within each device was investigated, as shown in Figure 2d–f. The work function of PDMS, serving as the dielectric, was measured as 5.82 eV (Figure S3). A schematic energy band diagram of the PDMS:Mg heterojunction is presented. Figure 2d, ii) illustrates the downward band bending of PDMS and the corresponding energy level alignment at the PDMS:Mg interface [29]. The schematic energy band diagram (Figure 2d, ii) qualitatively illustrates band alignment at equilibrium: due to the large work function difference ($\varphi_{PDMS} - \varphi_{Mg} = 2.79$ eV), electrons transfer from Mg to PDMS, establishing downward band bending and an interfacial dipole. This built-in potential enhances electron accumulation and trapping at the PDMS side during subsequent triboelectric charging cycles, contributing to the higher measured surface potential and TENG output of PM-TENG [30]. This band alignment facilitates efficient electron transfer across the heterojunction.

Furthermore, during repeated contact and separation between the Ni fabric tape and the PDMS:Mg layer, electrons from the Ni fabric tape transfer to the PDMS due to contact electrification. As a result, the overall electron transfer onto the PDMS is enhanced, leading to increased output performance of the TENG. This improvement arises from two complementary electron transfer mechanisms: one occurring at the polymer-electrode interface and the other driven by the contact electrification process itself.

However, as the work function difference between the dielectric and the metal electrode decreases, the amount of electron transfer onto PDMS via the electrode also diminishes. This was confirmed by the surface potential measurements, where PDMS:Zn (686 mV) and PDMS:Ni (269 mV) exhibited lower values than PDMS:Mg (1261 mV), as shown in Figure 2a–c. Consequently, although the electron transfer amount via contact electrification remains nearly the same, the output performance of TENG-PZ and TENG-PN is reduced due to the smaller work function differences of PDMS-Zn (2.13 eV) and PDMS-Ni (1.8 eV) compared to PDMS-Mg (2.79 eV).

The universality of this backside-electrode-induced mechanism was further verified by employing three alternative positively charged contact materials (Nylon 66, Al tape, and Cu tape; Figure S4). Across all three counter-materials, the PM > PZ > PN hierarchy is consistently preserved, while the absolute output scales with the tribo-positive strength of the counter-material, in agreement with the classical triboelectric series [31].

Based on the previous results, we propose the optimal electrode for enhancing the output performance of TENGs. While prior studies have primarily focused on engineering micro- and nanostructures on polymer surfaces, investigations addressing the interface between the polymer and electrode remain limited. To enhance the local stress distribution and interfacial coupling at the electrode-PDMS interface, we fabricated Mg electrodes with micropatterned surfaces by employing sandpapers of varying grit sizes (#120, #600, and #1000), selected to span the coarse, medium, and fine regions of the commercially available sandpaper spectrum, as shown in Figure 3a. This surface texturing is expected to improve interfacial contact and, consequently, triboelectric performance.

To compare the surface roughness of Mg before and after polishing with sandpapers, line scans and three-dimensional surface reconstructions were performed on Mg surfaces polished using #120, #600, and #1000 grit sandpapers, as shown in Figure 3b,c. The root mean square roughness (Rq) of Mg polished with #120 sandpaper was measured to be 1.73 μm, which is rougher than surfaces polished with #600 (0.89 μm) and #1000 (0.72 μm) sandpapers. This difference is attributed to the decreasing abrasiveness of the sandpaper as the grit number increases. Figure 3c presents three-dimensional surface images of pristine Mg and Mg scratched with the three different sandpapers, clearly illustrating the variation in surface texture.

We performed FEM simulations to quantify the effective stress (σ_{eff}) distribution within the PDMS layer, which directly governs the triboelectric surface charge density and, therefore, the TENG output as shown in Figure S1. The relationship between the simulated stress and the measured voltage is established through the following framework. First, the triboelectric surface charge density σ generated at the PDMS-Ni fabric interface depends on both the friction-interface work function gap $\Delta\varphi_1$ (electronic contribution) and the local effective stress σ_{eff} in the PDMS (mechanical contribution) [12, 25, 32]

$$\sigma \propto f(\sigma_{eff}) \cdot h(\Delta\Phi_1), \tag{1}$$

where f and h are monotonically increasing functions of stress and work function gap, respectively. The open-circuit voltage in contact-separation mode is given by equation [32]

$$V_{OC} = \sigma \cdot d/\varepsilon_0, \tag{2}$$

where d is the separation distance and ε_0 is the vacuum permittivity. Combining the two relations, V_{OC} is jointly controlled by σ_{eff} and $\Delta\varphi_1$ under fixed device geometry. In the Mg/Zn/Ni comparison (Figures 1 and 2), the electrode morphology is held constant so that variations in V_{OC} primarily reflect $h(\Delta\varphi_1)$ in the sandpaper series (Figure 4), $\Delta\varphi_1$ is fixed (all samples use Mg), and variations reflect (σ_{eff}). The FEM simulation therefore provides a quantitative link between the electrode morphology, which, via conformal PDMS coating, also determines the PDMS bottom geometry, and the local stress field within the PDMS. The enhancement mechanism is thus stress amplification through the coupled electrode-PDMS geometry, rather than a simple macroscopic contact area increase at the soft-elastomer interface, complementing the work function-driven contribution analyzed in Figures 1 and 2.

The width, length, and height of the cubes were set equal to the Rq roughness values of the polished Mg surfaces, as illustrated in Figure S1. Figure 4a–d, i) depict the effective stress distributions across the PDMS surface layers with varying roughness levels, subjected to an applied pressure of 25 kPa through an aluminum plate. The stress distribution profiles along the x-axis are also presented in Figure 4a–d, ii). Figure 4e summarizes the effective stress in PDMS for flat and micropatterned Mg samples polished with #120, #600, and #1000 sandpapers. Notably, the PDMS interfaced with the #120 polished Mg exhibits the highest effective stress (8.34 kPa), exceeding those with flat (7.16 kPa), #600 (7.25 kPa), and #1000 (4.4 kPa) polished Mg electrodes.

Furthermore, we measured the output performance of TENG-PM with varying electrode roughness. The TENG-PM device with the #120 polished Mg electrode exhibited the highest output voltage

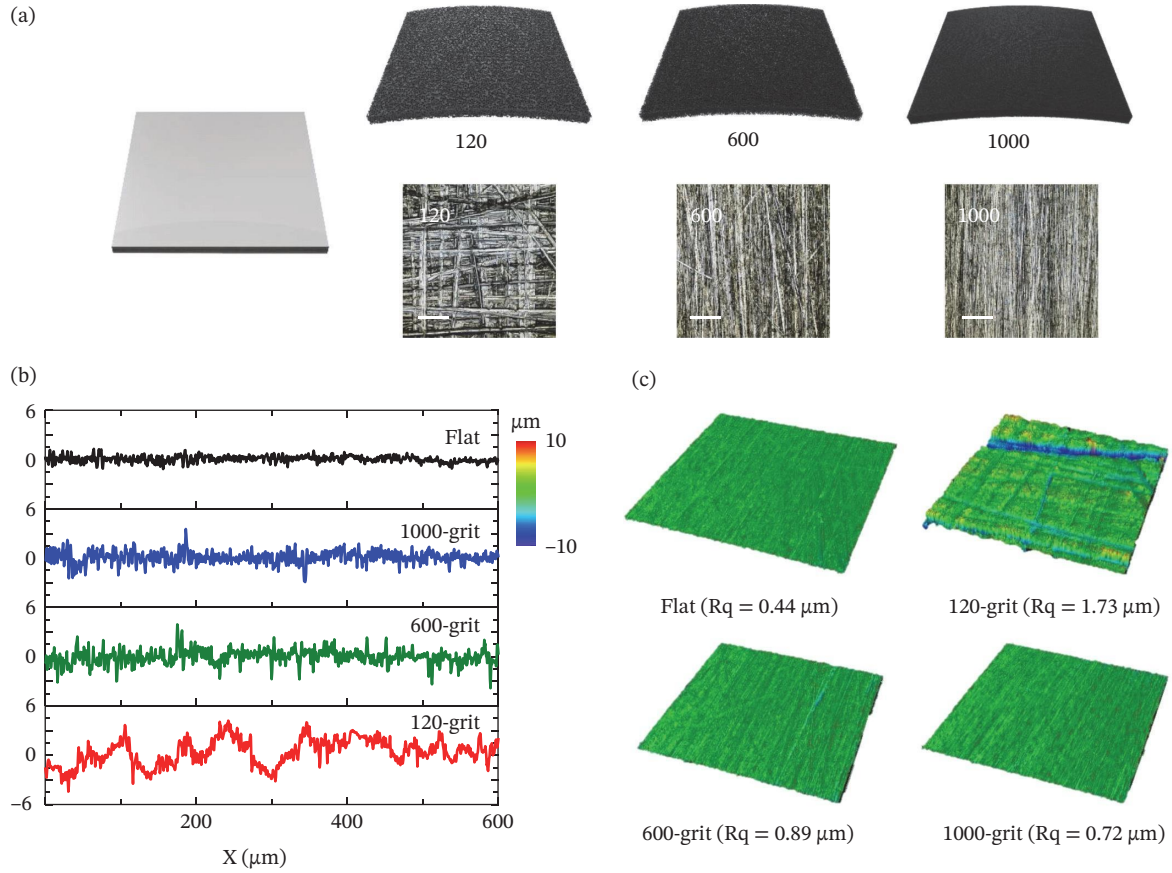

FIGURE 3 | Surface modification of micropatterned Mg using sandpapers. (a) Schematic of sandpapers with #120, #600, and #1000 grit and optical image of Mg (#120). Scale bars represent 400 μm. (b) Depth profile and (c) three-dimensional surface reconstructions obtained by confocal laser scanning microscopy (LSM; LEXT OLS4100, Olympus) of flat Mg, Mg (#1000), Mg (#600), and Mg (#120) surfaces.

(679.89 V), current (20.35 μA), and surface charge (39.66 nC) compared to other samples: flat Mg (532.07 V, 15.39 μA, 35.28 nC), #600 polished Mg (554.95 V, 17.10 μA, 35.29 nC), and #1000 polished Mg (372.00 V, 12.88 μA, 31.42 nC). The voltage hierarchy [#120 > #600 > flat > #1000] exhibits a one-to-one correspondence with the FEM-simulated effective stress hierarchy [#120 (8.34 kPa) > #600 (7.25 kPa) > flat (7.16 kPa) > #1000 (4.40 kPa)], directly confirming that the electrode roughness modulates the PDMS stress distribution and consequently the triboelectric charge generation.

To independently confirm that the roughness-induced output enhancement originates from the mechanical contribution rather than a shift in the electronic driving force, we measured the KPFM surface potential of all four PM samples (Figure S5). The surface potentials of PM flat (1261 mV), PM (#120) (1387 mV), PM (#600) (1324 mV), and PM (#1000) (1213 mV) fall within a narrow range, in contrast to the much larger variation in the PM/PZ/PN series (Figure 2). This confirms that the dominant electronic driving force ($\Delta\varphi_2$) is set by the backside metal type, while the patterned electrode introduces a secondary modulation through the mechanical stress field and electrode morphology. The TENG-PM (#120) configuration thus benefits from the combined action of the electronic contribution (large $\Delta\varphi_2 = 2.79$ eV from the Mg backside) and the mechanical contribution (maximal effective stress in PDMS), yielding the highest measured output.

Compared with prior micro-/nanostructural engineering of the PDMS polymer, which relies exclusively on mechanical stress enhancement at the friction interface, the proposed backside-electrode patterning approach combines both mechanical and electronic contributions (Table 2), achieving competitive output with a simpler and more scalable fabrication process.

The optimum output power of TENG devices is crucial for practical applications. We measured the output voltage and current of TENG-PM (#120) and TENG-PM across a range of external load resistances from 100 kΩ to 1 GΩ, as presented in Figure 5a,b. These experiments were conducted under a pushing pressure of 25 kPa, a working frequency of 4 Hz, and a gap distance of 4 mm. Figure 5a shows that as the external resistance increased, the output voltage of TENG-PM (#120) increased while the current decreased correspondingly. Specifically, the maximum voltage was 655.17 V for TENG-PM (#120) and 439.34 V for TENG-PM, while the maximum current reached 20.20 μA for TENG-PM (#120) and 15.30 μA for TENG-PM, as depicted in Figure 5a,b. The output power for both devices was calculated from measured current and external resistance using Equation (3).

$$P = I^2R, \tag{3}$$

where P is power, I is current, and R is the external resistance. The TENG-PM produced a maximum power output of 1.09 mW

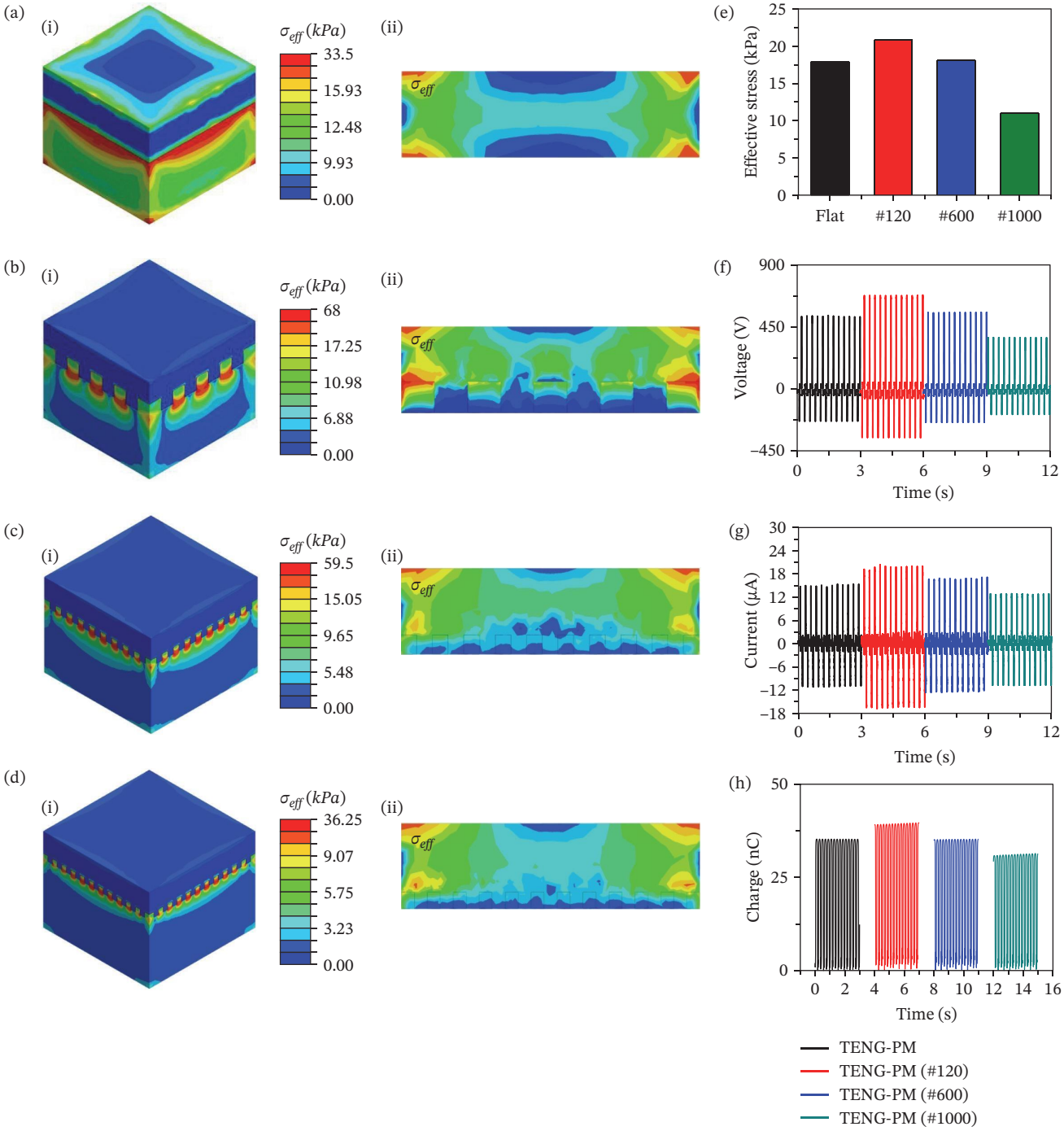

FIGURE 4 | Contour plots of simulated effective stress distribution in (a) PDMS-flat Mg, (b) PM (#120), (c) PM (#600) and (d) PM (#1000), including i) three-dimensional and ii) cross-sectional images of PDMS on flat Mg, Mg (#120), Mg (#600), and Mg (#1000). (e) Calculated effective stress values for flat Mg, Mg (#120), Mg (#600), and Mg (#1000). Output measurements: (f) voltage, (g) current, and (h) charge of TENG-PM, TENG-PM (#120), TENG-PM (#600), and TENG-PM (#1000).

at an external resistance of 6 MΩ. In comparison, TENG-PM (#120) achieved a higher maximum power output of 1.64 mW at an external resistance of 10 MΩ, representing approximately a 1.50-fold improvement over TENG-PM, as shown in Figure 5c.

Furthermore, we compared the capacitor charging capability of TENG-PM (#120) and TENG-PM using a 47 μF capacitor, as shown in Figure 5d. Figure S6 presents the rectified output voltage and current of TENG-PM (#120) measured through a bridge rectifier circuit. The TENG-PM (#120) generated a maximum voltage of 289 V and a current of 14.8 μA, demonstrating its superior charging performance under the tested conditions.

A 47 μF capacitor was charged using the rectified output from both TENG-PM (#120) and TENG-PM for 100 s. The TENG-PM (#120) charged the 47 μF capacitor to 0.91 V within 100 s, compared to 0.68 V by TENG-PM, showing the improved charging efficiency consistent with the enhanced output of the patterned device, as depicted in Figure 5d. Building on these results, TENG-PM (#120) was further tested by charging capacitors with capacitances of 22, 47, 68,

100, and 220 μF for 100 s, achieving voltages of 1.65, 0.91, 0.57, 0.37, and 0.19 V, respectively. The voltage decreases monotonically with increasing capacitance, consistent with the device's intrinsic source impedance and the characteristic RC charging behavior. Additionally, 100 light-emitting diodes (LEDs) connected in series were powered by the rectified output of TENG-PM (#120). Figure 5f illustrates the circuit schematic and the successful lighting of the 100 LEDs by TENG-PM (#120), demonstrating its robust energy harvesting capability.

A direct comparison with a conventional PDMS top-patterned control device (TENG-PM-top [#120]; Figure S7) further confirms that the backside-electrode patterning strategy achieves ~7% and ~16% higher peak voltage and current output under identical conditions, in addition to providing a mechanistically distinct electronic enhancement route via the metal-PDMS work function gap.

3 | Conclusions

This study systematically elucidates the critical role of electron transfer mechanisms at the interface between electrodes (Mg, Zn, and Ni) with different work functions and negatively charged materials (PDMS) in TENGs. By integrating material-specific work function differences between electrode and negatively charged material and finely tuning electrode surface morphology through controlled micropatterning, we demonstrate significant enhancements in electron transfer efficiency and mechanical stress distribution, directly translating to superior power generation performance. Our experimental investigations, supported by KPFM and FEM simulations, reveal that optimizing both the electronic and mechanical interface properties—exemplified by the micropatterned Mg electrodes (TENG-PM [#120])—maximizes output voltage, current, and power density, achieving a 1.28-fold enhancement in peak voltage and 1.50-fold enhancement in maximum output power compared to the unpatterned TENG-PM, with one-to-one correspondence between the measured voltage hierarchy and the FEM-predicted stress distribution. The combined action of the work function-driven interfacial polarization (electronic contribution) and the patterning-induced stress amplification (mechanical contribution) underlies the enhanced performance of the optimized TENG-PM (#120) devices. These findings advance the understanding of interfacial physics beyond classical electrostatic models, highlighting the interplay of band bending, work function alignment, and triboelectrification in governing charge dynamics. Consequently, this work provides a robust framework for designing next-generation TENGs with improved energy harvesting efficiency, paving the way for their broader application in wearable electronics, IoT systems, and sustainable energy solutions.

4 | Experimental

4.1 | Fabrication of the Metal Plates

Metal plates (Mg, Zn, and Ni), each with a thickness of 200 μm, were polished using #120, #600, and #1000 grit sandpaper. The polishing was performed manually by a single operator to ensure consistency. A cross-hatch abrasion pattern was employed: ~50 unidirectional strokes were applied, followed by a 90° rotation of the sample and another 50 strokes in the perpendicular direction, yielding an isotropic surface roughness. The total polishing

TABLE 2 | Comparison of TENG output enhancement strategies via interfacial engineering.

Refs.	Patterning approach	Patterning target	Mechanism	V_{max} (V)	I_{max} (μA)
Dudem 2017 [9]	Nanopillar array (AAO template)	PDMS top	Mechanical	568	25.6
Rasel and Park 2017 [33]	Sandpaper imprint	PDMS top via Al substrate	Mechanical	103 (peak-to-peak)	N/A
Park 2018 [19]	TiOx electron blocking layer	Interlayer between PDMS and electrode	Electronic (charge blocking)	272	9.1
Hwang 2021 [17]	Band-well structure (PDMS:ETL:PDMS)	PDMS internal	Electronic (charge trapping)	618	40.4
This work	Sandpaper polishing	Backside Mg electrode	Electronic + Mechanical	679.89	20.35

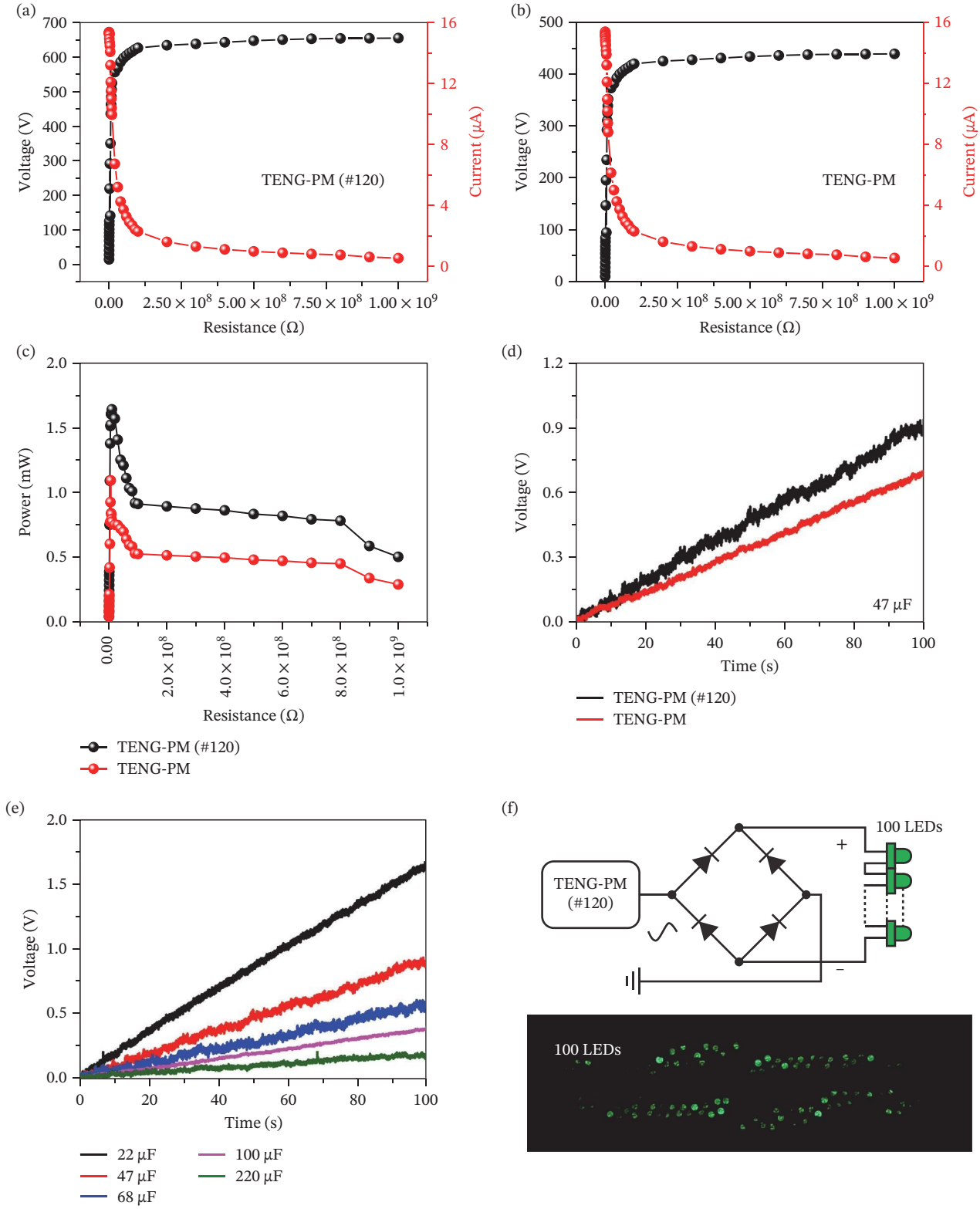

FIGURE 5 | Application of TENG-PM and TENG-PM (#120). Output voltage and current of (a) TENG-PM and (b) TENG-PM (#120) measured with external load resistances ranging from 100 kΩ to 900 MΩ. (c) Dependence of output power on external load for both TENG-PM and TENG-PM (#120). (d) Charging curve of a 47 μF capacitor by TENG-PM and TENG-PM (#120). (e) Charging curve of capacitors of 22 μF, 47 μF, 68 μF, 100 μF, and 220 μF using TENG-PM (#120). (f) Schematic of the circuit design including rectifying circuits and 100 green LEDs connected to TENG-PM (#120), along with a photograph showing the LEDs illuminated in the dark by TENG-PM (#120).

duration was ~5 min per sample, under moderate manual pressure maintained consistently throughout the process. Following the polishing process, the plates were cleaned via an ultrasonication bath in ethanol and acetone for 3 min each, with two cycles per solvent. The polished plates were then cut into the desired size (1 × 1 cm^2, 2 × 2 cm^2, and ASTM standard [type V]) using a nanosecond-pulse

ytterbium fiber laser (Biolino MOPA, Laservall) operating at a power of 20 W, a spot diameter of 60 μm, and a scanning speed of 1000 mm/s.

4.2 | Fabrication of Metal Plate Coating PDMS

The PDMS solution was prepared by mixing base resin and curing agent (Sylgard 184, Dow Corning Co.) at a weight ratio of 10:1. The resulting mixture was poured onto metal plates and subjected to a vacuum for 10 min to remove trapped air bubbles between the PDMS solution and the metal surface. The PDMS solution was then spin-coated onto the metal plate at 2000 rpm for 60 s. Subsequently, the coated metal plates were cured on a hot plate at 100°C for 2 h. This process yielded PDMS-coated metal plates with a uniform thickness of 50 μm.

4.3 | Measurement of TENG With Various Metal Plates and Characterization of Metal Plates

The output voltage, current, and charge were measured using an oscilloscope (MDO3052, Tektronix) equipped with a high-impedance probe (input impedance $Z_{probe} = 40\,M\Omega$), a low-noise current preamplifier (SR570, Stanford Research Systems), and an electrometer (6514, Keithley). For the output characterization under nominal conditions (Figure 4), the voltage was measured with the oscilloscope probe connected directly across the device, and the current was measured with the SR570 connected directly to the device under a quasi-short-circuit condition. For the load-dependent measurements (Figure 5), external load resistors (100 kΩ to 1 GΩ) were connected in series with the current preamplifier, while the oscilloscope probe remained connected in parallel across the device; the output power was calculated from the measured peak current as $P = I^2 \cdot R_{ext}$. The peak voltage and peak current values reported in Figures 4 and 5 are therefore measured under specific circuit configurations and should not be interpreted as ideal open-circuit voltage or short-circuit current. To minimize experiment environment variability, all TENG output measurements were performed under controlled ambient conditions (23°C, 10% RH). Samples compared within a single figure were measured within a single session under equivalent conditions to ensure comparability. All metal plates were prepared and tested according to the American Society for Testing and Materials (ASTM) standard (Test Method E8), using a strain elongation rate of 0.5 mm/min. Young's modulus was calculated from the slope of the stress (Budget Sensors). The tip work function (φ_{tip}) was calibrated against freshly cleaved highly oriented pyrolytic graphite (HOPG, $\varphi_{HOPG} = 4.6$ eV) [34]. The sample work function (φ_{sample}) was calculated from the measured contact potential difference (V_{CPD}) using the relation (1)

$$\Phi_{sample} = \Phi_{tip} + e \cdot V_{CPD}, \quad (4)$$

where e is the elementary charge. The V_{CPD} is reported following the Park Systems convention, $V_{CPD} = (\varphi_{sample} - \varphi_{tip})/e$, in which a positive V_{CPD} corresponds to a sample work function higher than that of the tip. All measurements on PM, PZ, and PN were performed on pristine PDMS-metal heterojunctions without prior tribo-charging so that the reported surface potential reflects the backside-electrode-induced interfacial polarization rather than accumulated triboelectric charges. For the intrinsic PDMS reference measurement (Figure S2), a 300-μm-thick PDMS film was cured on a grounded Au-coated glass substrate. The combination of the large PDMS thickness (~6 × that of the device) and the small Au-PDMS work function gap (0.72 eV) ensures that substrate-induced polarization is fully damped before reaching the top surface, allowing the measurement to represent the intrinsic PDMS work function. An AC voltage of 1 V at 17 kHz was applied to the atomic force microscope tip, and the $50 \times 50\,\mu m^2$ area was scanned at a rate of 0.3 Hz. 3D surface structures and roughness analysis were performed using confocal laser scanning microscopy (LSM; LEXT OLS4100, Olympus).

4.4 | Numerical Modeling and Simulations

To theoretically analyze the mechanical stress at the interface between PDMS and electrode, finite element method (FEM) simulations were performed using Midas NFX (Midas IT Co.). The interface roughness of Mg was simplified as a cubic structure. The theoretical models included PDMS and Mg with cubic features of 1.73×1.73, 0.89×0.89, and $0.72 \times 0.72\,\mu m^2$ at the interface between PDMS and Mg. For all mechanical FEM simulations, the pressure of 25 kPa was applied on the PDMS surface. Detailed simulation parameters and configurations are provided in the Figure S1.

Author Contributions

Minjung Chae contributed to methodology, investigation, experimentation, data analysis, and writing of the origin draft. June-Chul Shin contributed to substantial investigation, data analysis, FEM simulation, and review and editing. Hee Jae Hwang contributed to substantial investigation, data analysis, supervision, and writing – review and editing.

Funding

This work was financially supported by the National Research Foundation of Korea (NRF) grant funded by the Korea government (Grant RS-2022-NR072480).

Conflicts of Interest

The authors declare no conflicts of interest.

Data Availability Statement

The data that support the findings of this study are available upon request from the corresponding author. The data are not publicly available due to privacy or ethical restrictions.

References

1. A. Ahmed, I. Hassan, M. F. El-Kady, et al., "Integrated Triboelectric Nanogenerators in the Era of the Internet of Things," *Advanced Science* 6, no. 24 (2019): 1802230.

2. D. Choi, Y. Lee, Z.-H. Lin, et al., "Recent Advances in Triboelectric Nanogenerators: From Technological Progress to Commercial Applications," *ACS Nano* 17 (2023): 11087–11219.

3. F. Haihang, X. Yu, Y. Wenjie, et al., "Maskless Formation of Patterned Leather-Based Conductive Electrode for Human-Computer Interaction Application," *Energy Materials* 5, no. 9 (2025): 500112.

4. H. J. Hwang, J. S. Yeon, Y. Jung, H. S. Park, and D. Choi, "Extremely Foldable and Highly Porous Reduced Graphene Oxide Films for Shape-Adaptive Triboelectric Nanogenerators," *Small* 17, no. 9 (2021): 1903089.

5. H. Park, S.-J. Oh, M. Kim, et al., "Plasticizer Structural Effect for Sustainable and High-Performance PVC Gel-Based Triboelectric Nanogenerators," *Nano Energy* 114 (2023): 108615.

6. H. J. Hwang, D. Kwon, H.-Y. Kwon, M. Shim, J. M. Baik, and D. Choi, "Integrated System of Mechanical Regulator and Electrical Circuitry on Triboelectric Energy Harvesting With Near-Field Communication for Low Power Consumption," *Advanced Energy Materials* 15, no. 2 (2025): 2400481.

7. H. J. Hwang, J. S. Kim, W. Kim, et al., "An Ultra-Mechanosensitive Visco-Poroelastic Polymer Ion Pump for Continuous Self-Powering Kinematic Triboelectric Nanogenerators," *Advanced Energy Materials* 9, no. 17 (2019): 1803786.

8. Y. Xiao, J. Lu, and B. Xu, "Synergistic Effect Study of g-C_3N_4 Composites for High-Performance Triboelectric Nanogenerators," *Energy Materials* 5 (2025): 500057.

9. B. Dudem, N. D. Huynh, W. Kim, et al., "Nanopillar-Array Architectured PDMS-Based Triboelectric Nanogenerator Integrated With a Windmill Model for Effective Wind Energy Harvesting," *Nano Energy* 42 (2017): 269–281.

10. T. Cheng, J. Shao, and Z. L. Wang, "Triboelectric Nanogenerators," *Nature Reviews Methods Primers* 3 (2023): 39.

11. Z. L. Wang, "From Contact Electrification to Triboelectric Nanogenerators," *Reports on Progress in Physics 84* (2021): 096502.

12. Z. L. Wang and A. C. Wang, "On the Origin of Contact-Electrification," *Materials Today* 30 (2019): 34–51.

13. H. Zhao, H. Wang, H. Yu, et al., "Theoretical Modeling of Contact-Separation Mode Triboelectric Nanogenerators From Initial Charge Distribution," *Energy & Environmental Science* 17, no. 6 (2024): 2228–2247.

14. O. L. A. Monti, "Understanding Interfacial Electronic Structure and Charge Transfer: An Electrostatic Perspective," *The Journal of Physical Chemistry Letters* 3, no. 17 (2012): 2342–2351.

15. J.-K. Kim, G. H. Han, S.-W. Kim, et al., "Electric-Field-Driven Interfacial Trapping of Drifting Triboelectric Charges via Contact Electrification," *Energy & Environmental Science* 16, no. 2 (2023): 598–609.

16. H. J. Hwang, J. S. Kim, S. Oh, et al., "Self-Powered Real-Time Temperature Sensing Based on Flexible Ionic Elastomer on Triboelectric Nanogenerators," *Advanced Functional Materials* 35, no. 50 (2025): e04081.

17. H. J. Hwang, H. Hong, B. G. Cho, et al., "Band Well Structure With Localized States for Enhanced Charge Accumulation on Triboelectrification," *Nano Energy* 90 (2021): 106647.

18. Y. Zou, J. Xu, K. Chen, and J. Chen, "Advances in Nanostructures for High-Performance Triboelectric Nanogenerators," *Advanced Materials Technologies* 6, no. 3 (2021): 2000916.

19. H.-W. Park, N. D. Huynh, W. Kim, et al., "Electron Blocking Layer-Based Interfacial Design for Highly-Enhanced Triboelectric Nanogenerators," *Nano Energy* 50 (2018): 9–15.

20. J. Wu, X. Wang, H. Li, F. Wang, W. Yang, and Y. Hu, "Insights Into the Mechanism of Metal-Polymer Contact Electrification for Triboelectric Nanogenerator via First-Principles Investigations," *Nano Energy* 48 (2018): 607–616.

21. M. Stössel, J. Staudigel, F. Steuber, J. Simmerer, and A. Winnacker, "Impact of the Cathode Metal Work Function on the Performance of Vacuum-Deposited Organic Light Emitting-Devices," *Applied Physics A: Materials Science & Processing* 68, no. 4 (1999): 387–390.

22. B. Ofuonye, J. Lee, M. Yan, C. Sun, J.-M. Zuo, and I. Adesida, "Electrical and Microstructural Properties of Thermally Annealed Ni/Au and Ni/Pt/Au Schottky Contacts on AlGaN/GaN Heterostructures," *Semiconductor Science and Technology* 29, no. 9 (2014): 095005.

23. W. Melitz, J. Shen, A. C. Kummel, and S. Lee, "Kelvin Probe Force Microscopy and Its Application," *Surface Science Reports* 66, no. 1 (2011): 1–27.

24. S. Sadewasser and T. Glatzel, "Kelvin Probe Force Microscopy From Single Charge Detection to Device Characterization: From Single Charge Detection to Device Characterization," (2018).

25. S. Paria, S. K. Si, S. K. Karan, et al., "A Strategy to Develop Highly Efficient TENGs Through the Dielectric Constant, Internal Resistance Optimization, and Surface Modification," *Journal of Materials Chemistry A* 7, no. 8 (2019): 3979–3991.

26. C. Wang, H. Guo, P. Wang, J. Li, Y. Sun, and D. Zhang, "An Advanced Strategy to Enhance TENG Output: Reducing Triboelectric Charge Decay," *Advanced Materials* 35, no. 17 (2023): 2209895.

27. H. J. Hwang, Y. Choi, S. Kim, et al., "Synergistic Integration of Electrical Stimulation, Reactive Oxygen Species Regulation, and Pro-Angiogenic for Accelerated Wound Healing," *Nano Energy* 131 (2024): 110200.

28. J. Tian, Y. He, F. Li, W. Peng, and Y. He, "A Comprehensive Review on the Mechanism of Contact Electrification," *Journal of Materials Chemistry A* 13, no. 4 (2025): 2505–2536.

29. H. Zou, L. Guo, H. Xue, et al., "Quantifying and Understanding the Triboelectric Series of Inorganic Non-Metallic Materials," *Nature Communications* 11 (2020): 2093.

30. D. Li, C. Wu, L. Ruan, et al., "Electron-Transfer Mechanisms for Confirmation of Contact-Electrification in ZnO/Polyimide-Based Triboelectric Nanogenerators," *Nano Energy* 75 (2020): 104818.

31. W. Seung, M. Gupta, K. Lee, et al., "Nanopatterned Textile-Based Wearable Triboelectric Nanogenerator," *ACS Nano* 9, no. 4 (2015): 3501–3509.

32. S. Niu and Z. L. Wang, "Theoretical Systems of Triboelectric Nanogenerators," *Nano Energy* 14 (2015): 161–192.

33. M. S. U. Rasel and J.-Y. Park, "A Sandpaper Assisted Micro-Structured Polydimethylsiloxane Fabrication for Human Skin Based Triboelectric Energy Harvesting Application," *Applied Energy* 206 (2017): 150–158.

34. W. N. Hansen and G. J. Hansen, "Standard Reference Surfaces for Work Function Measurements in Air," *Surface Science* 481, no. 1–3 (2001): 172–184.

Supporting Information

Additional supporting information can be found online in the Supporting Information section. **Supporting Information.** The Supporting Information provides additional experimental and analytical details, including Figure S1: simulation information, Figure S2: schematic of our TENG, Figure S3: PDMS work function, Figure S4: TENG output voltage and current, Figure S5: surface potential of PMs (flat, #120, #600, and #1000), Figure S6: output voltage and current before and after rectifying, and Figure S7: comparison of the output via backside-electrode pattering and top surface patterning.